JOURNAL OF MATERIALS SCIENCE 14 (1979) 1413–1420

# Fracture of a brittle particulate composite

## Part 1 *Experimental aspects*

DAVID J. GREEN
*Ceramic Section, Mineral Sciences Laboratories, Canada Centre for Mineral and Energy Technology, Department of Energy, Mines and Resources, Ottawa, Ontario, Canada*

PATRICK S. NICHOLSON, J. DAVID EMBURY
*Department of Metallurgy and Material Sciences, McMaster University, Hamilton, Ontario, Canada*

A study was made of the fracture process in a model brittle composite containing nickel spheres in a glass matrix. The macroscopic fracture characteristics of the system were determined by fracture surface energy, fracture strength and elastic modulus measurements. The microstructures of the composites were defined using quantitative microscopy and the fracture process was studied by the technique of ultrasonic fractography. This procedure traced changes in the crack front configuration and local crack velocity as the crack interacted with the array of nickel particles.

### 1. Introduction

It is well known that the presence of inclusions and internal boundaries can lead to increases in fracture toughness of brittle solids. Although a variety of mechanisms have been proposed to explain the observed increases, the validity of a number of these mechanisms remains to be demonstrated.

The role of inclusions in the fracture of highly brittle solids can be considered in a variety of ways. In the original Griffith's concept, the major energy-absorbing process is the production of surface energy ($\Gamma$) [1] and thus, increase of total relative fracture surface increases toughness. In particulate composites, mechanisms such as surface step formation [2] and surface roughness [3] increase the fracture surface area. An increase in fracture surface area will also occur when a microcrack zone is produced in the vicinity of the crack tip [4], due to the decohesion of internal boundaries, or arrested failure of the matrix or the particles.

An alternative approach is to consider the changes in the crack-tip stress field due to the presence of the inclusions. For example, the presence of the particles on or near the crack plane can impede the motion of a crack and hence change the crack-front configuration. Impedance to crack motion could result from the particles being tougher or from the local stresses around the particles due to thermal expansion or elastic mismatch. The concept that crack bowing could lead to increased fracture toughness was first postulated by Lange [5]. In this and subsequent analyses [6–7] it was assumed that the local increase in crack resistance is reflected by the change of crack shape which, in turn, is used to calculate the change in the critical strain energy release rate ($G_c$). To date, however, relatively little attention has been paid to experimentally determining changes in crack-front configuration. The primary aim of this work is to study the variations of crack-front shape in a systematic way using ultrasonic fractography. This technique was developed by Kerkhof and co-workers for crack velocity measurement in brittle solids [9]. It involves the transmission of a beam of transverse ultrasonic waves through a sample at the time of fracture. The oscillating shear wave produces a mode II stress intensity component at the crack front, which modulates the path of a growing crack, leaving a ripple

TABLE I Physical properties of the starting powders

| Powder | Density ($g\,cm^{-3}$) | Particle size ($\mu m$) | Coefficient of Linear Expansion ($10^6\,°C^{-1}$)* |
|---|---|---|---|
| Nickel | 8.87 | 132 | 13.9 |
| S-glass‡ | 2.51 | – | 13.8 |

* Stett and Fulrath [12].
† The size distribution was identified as being log-normal by SEM projected diameters.
‡ Nominal composition (wt %) 55 $SiO_2$, 30 $Na_2O$, 15 $Al_2O_3$.

marking on the fracture surface. As the frequency of the imposed wave is known, the crack velocity can be determined from the ripple spacing and detailed information on crack shape changes in the vicinity of second phase particles can be obtained [10, 11].

For this study, a model brittle composite of nickel spheres in a glass matrix was chosen. This is a model system, because the interfacial strength, thermal expansion mismatch, particle size and shape can be controlled [12]. The fracture mechanisms were studied by fractography and local changes in the crack-front configuration were studied by ultrasonic fractography.

## 2. Experimental procedure

S glass (composition Table I) has approximately the same thermal expansion coefficient as nickel and does not adhere to unoxidized nickel [13, 14]. The physical properties of the glass and nickel are also given in Table I.

Samples containing 2, 4, 6, 10, 15 and 20 vol % nickel and S-glass power were vacuum hot-pressed in graphite dies at 680° C at a pressure of 7 MPa to > 99% theoretical density. Following an anneal at 500° C, DCB fracture specimens (51 mm x 13 mm x 6 mm with 2 mm sidegrooves), were diamond-machined from the hot-pressed discs. An end notch, (~ 10 mm) was introduced into the sample. Pre-cracking was accomplished with a wedge-loading device. Special pre-drilled, metal loading tabs were glued to the ends of the DCB samples. The sample geometry is shown in Fig. 1. Following machining, the samples were re-annealed at 450° C.

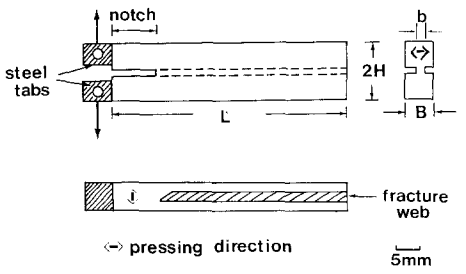


*Figure 1* Machining details for DCB fracture samples showing specimen size and notch configuration.

The Young's moduli of the composites were determined from the longitudinal sound velocity in the samples and from load–deflection data. Fracture surface energy values ($\Gamma$) were determined using the DCB testing geometry. The DCB rig was designed to reduce friction loads and to ensure accurate alignment of the samples [15]. Fracture surface energy values were determined from critical load–deflection measurements using,

$$G_I = \frac{1}{b}\left(\frac{27P^4\delta^2}{EBH^3}\right)^{1/3}, \quad (1)$$

where $P$ is the load, $B$ the beam breadth, $H$ its height, $b$ the web width, and $\delta$ the total deflection of both cantilever beams [15]. At fracture, the critical value of $G_I$ is equal to $2\Gamma$. This approach was preferred as accurate crack length measurement was difficult in these composites. The DCB tests were carried out on an Instron Universal testing machine (cross-head speed, 0.05 mm $min^{-1}$) and an extensometer measured the deflection. To check accuracy, standard samples of Pyrex were also tested and results compared with literature values (± 2% obtained). The fracture strength was determined by four-point bending using sample halves previously produced in the DCB testing. The inner and outer loading spans were 25 and 38 mm, respectively. Samples from the strength tests were subsequently viewed by optical and scanning electron microscopy to study the fractographic features.

Finally, a series of DCB samples were used for the ultrasonic fractography experiments. A water-cooled transducer containing a Y-cut quartz crystal with a basic frequency of 1 MHz, driven by a 1 kW transmitter, was mounted on the end of the DCB sample so that the crack propagated towards it. This geometry gives rise to a Doppler shift in the frequency of the ultrasonic wave but as crack speeds were typically less than 50 m $sec^{-1}$, no

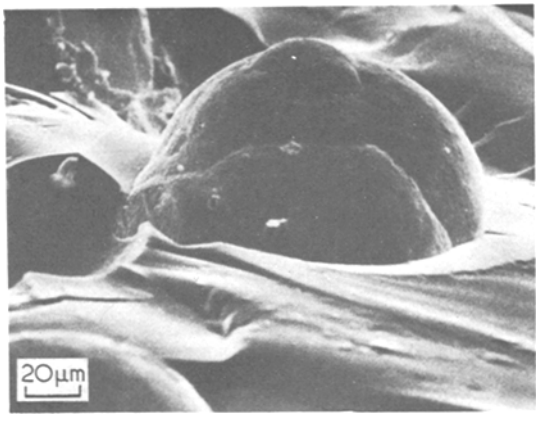


*Figure 2* Side view of fracture surface showing the intersection of a nickel sphere by the crack front (SEM).

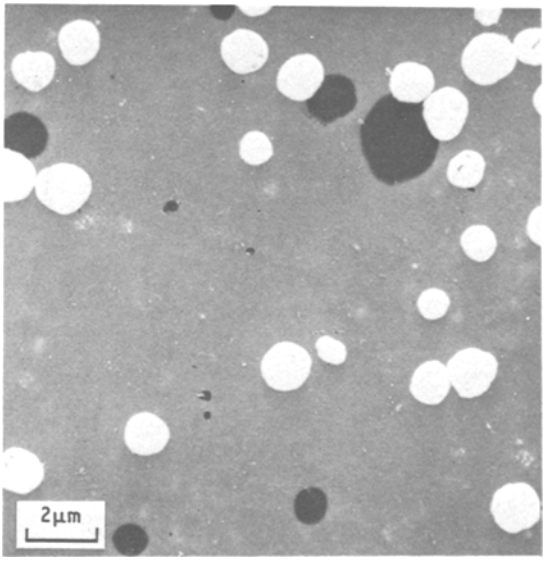


*Figure 3* Optical micrograph of a polished section; S-glass–10% nickel.

frequency correction was necessary. The ultrasonic equipment and further details of the experimental procedure are given elsewhere [16]. Fractographic observations were made on the ultrasonically modulated samples using scanning electron and interference microscopy. For electron microscopy, the samples were coated with carbon and shadowed at $\sim 5^{\circ}$ to the surface. For the interference microscopy, the samples were coated with a thin layer of gold.

## 3. Results and discussion

### 3.1. Microstructural definition

Theoretical calculations of the critical strain energy release rate for a crack impeded by an array of impenetrable obstacles has shown it to be a function of the ratio of the particle diameter ($2r$) to the inter-obstacle spacing ($d$) [6]. The particles are not all one size, however, but a distribution of sizes. To resolve this and other problems, it was assumed that the overall fracture process can be defined in terms of the average particle size and that the sectioning of the particles is determined by the strain field around them [17]. For non-bonded obstacles with no self-stresses, the crack front will be attracted to the particles due to an elastic modulus interaction and will tend to sample the maximum particle diameter. This concept was supported by fractographic observations (Fig. 2).

The degree of dispersion ($d_p$) of the nickel particles was estimated using quantitative microscopy and the particle-size distribution before and after fabrication was compared. The Schwarz–Saltykov method was used to determine the particle-size distribution after fabrication. The distribution of particle diameters on plane polished sections, such as illustrated in Fig. 3, was measured [18]. The comparison of the average particle size before ($2r_b$) and after fabrication ($2r_a$) is given in Table II. There is an apparent increase in size after fabrication. This effect is explained by interparticle contact ($d_p$ decreases) and examples of this can be seen in Fig. 3. The average value of $r$ was increased by 14% for a 20 vol % sample.

For interaction with very weak obstacles, the crack front will remain virtually straight and the average value of $d$ will be equivalent to the mean free path ($d_w$):

$$d_w = \frac{L_3(1 - V_v)}{V_v}, \qquad (2)$$

where $V_v$ is the volume fraction of particles and $L_3$ is the average particle intercept length. For strong obstacles, however, the crack front will curve and it will sample more obstacles per unit length than expected for a random straight line. In this case the value of $d$ will be less than $d_w$.

TABLE II Comparison of average particle size before and after fabrication

| Volume fraction nickel | $2r_b$ (μm) | $2r_a$ (μm) | $d_p$ |
|---|---|---|---|
| 0.06 | 132 | 146 | 0.94 |
| 0.10 | 132 | 147 | 0.92 |
| 0.15 | 132 | 148 | 0.88 |
| 0.20 | 132 | 150 | 0.85 |

TABLE III Comparison of interobstacle distance for strong and weak obstacles

| Volume fraction nickel | $d_w$ (μm) | $N_A$ (mm)$^{-2}$ | $d_s$ (μm) | $2r$ (μm) | $2r/d_w$ | $2r/d_s$ |
|---|---|---|---|---|---|---|
| 0.06 | 1430 | 5.81 | 269 | 146 | 0.10 | 0.54 |
| 0.10 | 805 | 9.66 | 175 | 147 | 0.18 | 0.84 |
| 0.15 | 536 | 16.36 | 90 | 148 | 0.28 | 1.49 |
| 0.20 | 336 | 20.36 | 72 | 150 | 0.45 | 2.08 |

For strong obstacles, a useful approximation for interobstacle spacing ($d_s$) is:

$$d_s = N_A^{-1/2} - 2r, \quad (3)$$

where $N_A$ is the number of particles per unit area [19]. The second term accounts for the finite size of the particles. Table III lists the quantitative microscopic measurements for the S-glass–nickel system. It can be seen that differences between $d_s$ and $d_w$ are pronounced.

## 3.2. Fracture properties of the S-glass–nickel system

The sonically determined values of Young's modulus for the glass–nickel composites are shown in Fig. 4. Also included are the predicted values of $E$ assuming well-bonded particles [20], non-bonded particles [21] or voids [22]. The decrease in the measured values of $E$ indicates non-bonded interfaces, as originally projected in the microstructural design. These non-bonded particles are sometimes referred to as "pseudovoids".

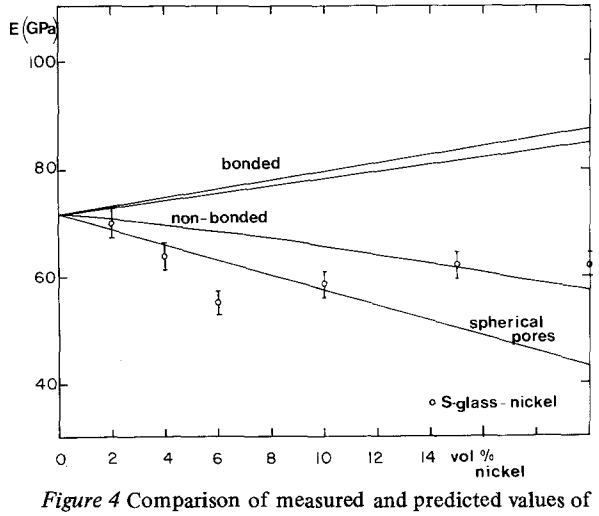


*Figure 4* Comparison of measured and predicted values of Young's modulus for the S-glass–nickel system.

The value of the critical stress intensity factor ($K_{IC}$) for Pyrex tested in air at room temperature, using load–crack length data, was found to be $0.76 \pm 0.02\,MN\,m^{-3/2}$. Literature values of $K_{IC}$ range between 0.764 to $0.77\,MN\,m^{-3/2}$ depending on the test conditions [23]. The agreement with the literature indicated the reliability of the DCB rig.

The mechanical properties of the glass–nickel composites are presented in Table IV. Calculated values of the critical flaw size are larger than the average particle size (0.13 mm), suggesting that the stress fields associated with the particles assist the subcritical growth of existing flaws in the glass matrix. For the non-bonded particles, the elastic modulus stress field would tend to promote radial cracking between particles and hence increase the critical flaw size.

The fracture resistance was also monitored continuously in the DCB testing. Fig. 5 shows a comparison of the crack resistance($R$)–crack length measurements for S-glass and S-glass–10% nickel samples. For the 10% nickel sample, the curve exhibits several undulations, reflecting the variable resistance to crack propagation.

## 3.3. Fractographic observations

Fractographic observations were made on the flexure samples to locate fracture origins. The

TABLE IV Fracture properties of the S-glass–nickel system

| Volume fracture nickel | $E$ (GPA) | $\sigma_f$ (MPa) | ($J\,m^{-2}$) | $c$ *(mm) |
|---|---|---|---|---|
| 0.00 | 72 | 53 | 4.8 | 0.19 |
| 0.06 | 55 | 41 | 9.3 | 0.58 |
| 0.10 | 59 | 40 | 10.1 | 0.62 |
| 0.15 | 62 | 35 | 10.5 | 0.10 |
| 0.20 | 62 | 39 | 10.1 | 0.85 |

* Assumption of penny-shaped flaw ($Y = (4/\pi)^{1/2}$).

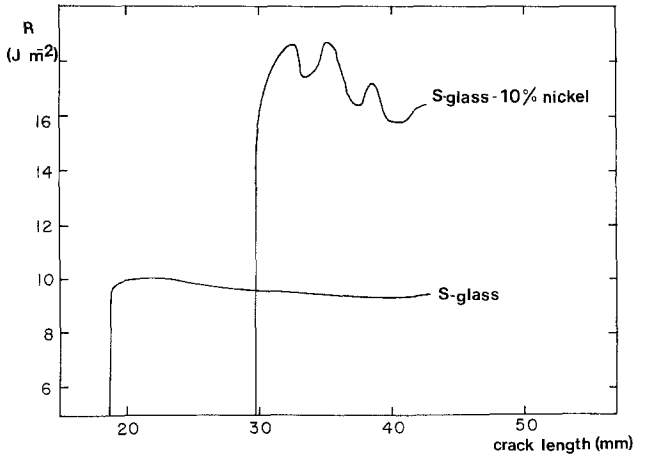


*Figure 5* Crack resistance curves for S-glass and S-glass–10 vol % nickel samples.

fracture origin was typically located near the tensile surface and in the vicinity of two contacted nickel spheres.

Fractographic observation of the DCB samples clearly indicated the nickel produced an increased surface roughness, (less than 20% for a 20 vol % sample) particularly local to the particles.

Fractographic evidence indicated changes of crack direction on approach to the nickel particles especially at low volume fractions. In some cases this left a distinct ledge in front of the particles (Fig. 6). Finally, no evidence of secondary cracking was found either between particles or at the glass–nickel interface and no glass adhered to the nickel particles following fracture.

More detail of the local crack-particle interactions was obtained from the ultrasonic investigations. Fig. 7 clearly shows that the nickel spheres act to impede the motion of the crack as it by-passes the sphere. The crack velocity (ripple-spacing) is a minimum at the centre of

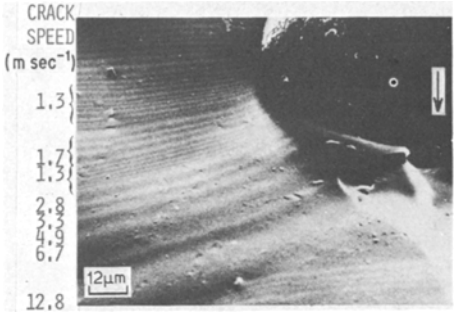


*Figure 7* Ultrasonic fractograph of S-glass–2% nickel sample as observed in SEM.

the obstacle and then increases up to breakaway. The secondary cracks at this point are non-coplanar and leave a fracture surface step behind the particle. There is also evidence of the crack being "attracted" to the nickel particles during approach (Fig. 8). At higher volume fractions, the ripple markings become less distinct, but

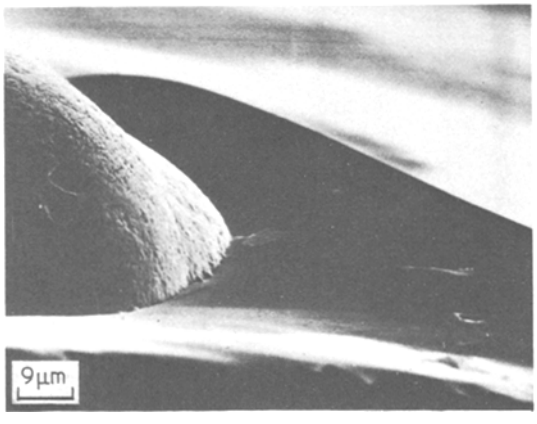


*Figure 6* Side view of a fracture surface showing abrupt change in crack direction prior to particle interaction.

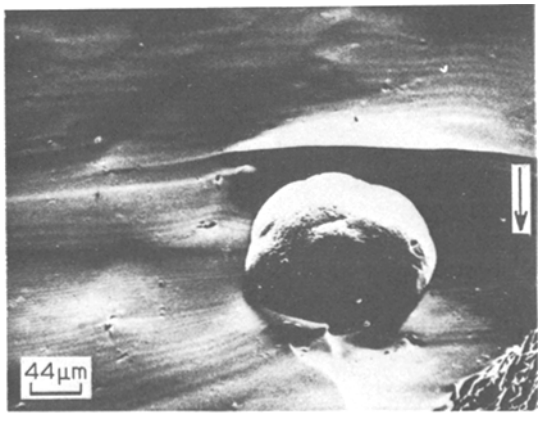


*Figure 8* SEM display of crack front approaching, intersecting and departing from a nickel particle.

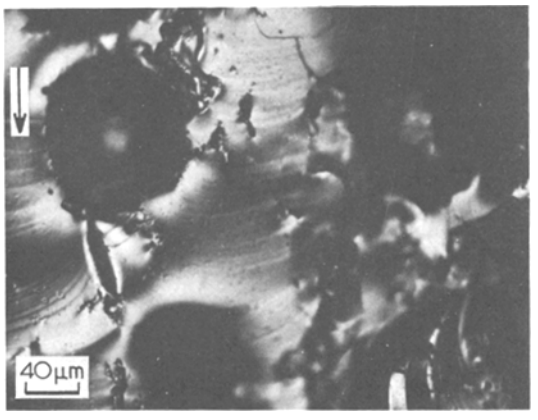


*Figure 9* Ultrasonic fractograph for a S-glass–6% nickel sample (Nomarksi interference).

Nomarski interference microscopy improved these observations (Fig. 9). Quantitative measurements of the change of crack-front configuration and local crack velocity were made. The remnant fracture surface steps also impede crack motion but this disturbance was less pronounced. These observations are similar to those for the S-glass–pore system [11] due to the non-bonded nature of the nickel particles.

### 3.4. Fracture mechanisms

The variation in $\Gamma$ observed in these composites can be related to the fracture mechanisms discussed earlier. As the nickel spheres are non-bonded there is no plastic contribution to $\Gamma$. Failure of the nickel particles or their decohesion also plays no role. Fractographic observations show that although the nickel particles did increase the surface roughness, this increase is insufficient to explain the increase in $\Gamma$. Similarly, no evidence was found of microcracking between the nickel particles. The increase in $\Gamma$ must, therefore, be related to the crack–particle interactions.

It has been suggested that the formation of the fracture surface steps might involve a major expenditure of energy as they do not form under mode I loading [2]. This step contribution to $\Gamma$ ($\Gamma_s$) can be estimated from

$$\Gamma_s = \tfrac{1}{2}\tau(h^2/s) \qquad (4)$$

where $\tau$ is the shear stress acting during step formation and $s$ is the step spacing. It is assumed that the displacement needed to form the step is the step height. Actually, the fracture step, which is curved, is formed under a complex combination of normal and shear stresses so the displacement needed is probably much smaller than given by Equation 4 and could be as low as the average Si–O bond length ($a_o$). A more reasonable estimate of the step contribution is

$$\Gamma_s = \tfrac{1}{2}\tau(h/s)a_o. \qquad (5)$$

Substituting values of $\tau = 10\,\text{GPa}$, $h = 60\,\mu\text{m}$, $a_o = 0.2\,\text{mn}$ and $s = 250\,\mu\text{m}$ into Equations 4 and 5 for a 20 vol % nickel samples gives $\Gamma_s = 7.2 \times 10^4$ and $\Gamma_s = 0.24\,\text{J m}^{-2}$ respectively. The former estimate is several orders of magnitude greater than any of the observed $\Gamma$ values while the latter is approximately 5% of the fracture surface energy of the S-glass. This latter value is in good agreement with the fractographic estimate of surface roughness. It appears, therefore, that the energy involved in step formation is small. There is evidence from the S-glass–pore system, however, that these steps may be left as ligaments behind the major crack front [11]. Such would increase $\Gamma_s$ by increasing the step density and

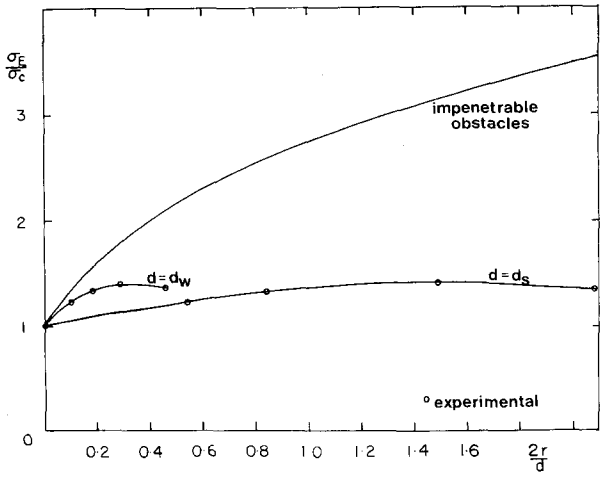


*Figure 10* Comparison of experimental results for S-glass–nickel system with theoretical prediction for interaction of crack with impenetrable obstacles.

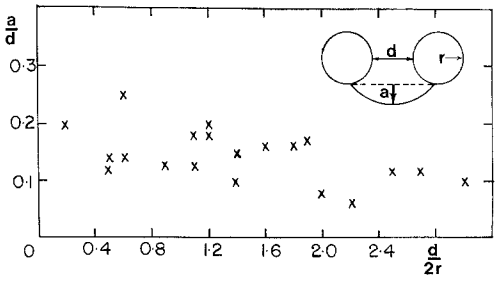


*Figure 11* Observed critical crack shape at breakaway.

also the displacement needed to fracture the step.

For the local crack/particle interactions, the ultrasonic fractography clearly indicates the major perturbation of the crack front to occur as it bypasses the nickel spheres. A minor perturbation also occurs as it moves past the residual fracture steps, indicating that there is probably some contribution to $\Gamma$ from their formation.

If $\sigma_E$ is the critical stress needed to move the curved crack front between the obstacles and $\sigma_c$ is the stress needed to move the crack front in the absence of any obstacles, Fig. 10 shows a comparison of the measured variation in $\sigma_E/\sigma_c$ and that predicted for semi-elliptical, non-interacting segmented cracks interacting with impenetrable obstacles [6]. It can be shown that

$$\frac{\sigma_E}{\sigma_c} = \frac{(E\Gamma)^{1/2}}{E_o \Gamma_o} \quad (6)$$

where $E_o$ and $\Gamma_o$ are the Young's modulus and fracture surface energy of the non-dispersed glass. The experimental data are shown in Fig. 11 for the two extreme definitions of $d$ discussed earlier. In neither case can the particles be considered impenetrable but they may be acting as weak obstacles to crack propagation. In the theoretical approach it is assumed that the crack is pinned to the front of the obstacle and must bow completely round the obstacle before it breaks away [6]. Ultrasonic fractography indicates that this type of process does not occur for the non-bonded nickel particles. Finally, Fig. 11 shows the measured values of crack shape at breakaway for the S-glass–nickel systems. There is a large scatter in the data but there appears to be an increase in crack curvature as the volume fraction increases. This is in qualitative agreement with theoretical predictions [6].

## 4. Conclusions

The fracture process and local crack–particle interactions of an S-glass–nickel sphere composite have been studied. Fracture measurements showed that there was slight decreases in Young's modulus values and fracture strength as the volume fraction of nickel increased. There was a marked decrease in both the fracture surface energy and calculated critical flaw size values as the nickel volume fraction increased. The experimental design considered the particles non-bonded and this was supported by the drop in Young's modulus and the fractography.

Fractographic observations were used to assess the various fracture mechanisms that could be involved in the fracture process. It was determined that increases in surface roughness, fracture step formation, microcracking and plasticity could not explain the experimental observations. Ultrasonic fractography illustrated the nature of the local interaction between the crack front and the particles which clearly impede the crack and change the crack-front configuration. It is proposed that this local impedance to crack motion increases the critical strain energy release rate and hence the fracture toughness of the system. Comparison with theory, however, showed that non-bonded nickel spheres acted as relatively weak obstacles.

## Acknowledgements

The work was sponsored by the Atomic Energy of Canada Ltd. The authors would like to acknowledge Dr F. Kerkhof and Martin Schinker of the Ernst Mach Institute in Freiburg and R. G. Hoagland of Battelle-Columbus, Ohio.

## References

1. A. A. GRIFFITH, *Phil. Trans. Roy. Soc.* 221A (1920) 163.
2. C. N. AHLQUIST, *Acta Met.* 23, (1975) 239.
3. S. M. WIEDERHORN, "Mechanical and Thermal Properties of Ceramics", NBS Spec. Publ., (1969) p. 217.
4. R. G. HOAGLAND, G. T. HAHN and A. R. ROSENFELD, *Rock Mech.* 5 (1973) 77.
5. F. F. LANGE, *Phil. Mag.* 22, (1970) 983.
6. A. G. EVANS, *ibid* 26 (1972) 1327.
7. A. G. EVANS and L. J. GRAHAM, *Acta Met.* 23 (1975) 1303.
8. A. G. EVANS, A. H. HEUER and D. L. PORTER, "Fracture 1977", Vol. 1, edited by D. M. R. Taplin, (University of Waterloo Press, 1977) pp. 529.
9. F. KERKHOF, "Bruchvorgange in Glasern" (Verlag dur Deut. Glastech. Ges., 1970).
10. K. PETER, *Z. Agnew, Phys.* 25 (1968) 309.
11. D. J. GREEN, P. S. NICHOLSON and J. D. EMBURY, *J. Mater. Sci.* 12 (1977) 987.

12. M. A. STETT and R. M. FULRATH, *J. Amer. Ceram. Soc.* **53** (1970) 5.
13. D. O. NASON, M.S. Thesis, University of California, Berkeley (1962).
14. R. L. BERTOLOTTI and R. M. FULRATH, *J. Amer. Ceram. Soc.* **50**, (1967) 558.
15. R. G. HOAGLAND, C. W. MARSHALL and A. R. ROSENFELD, *Mater. Sci. Engg.* **15** (1974) 51.
16. D. J. GREEN, Ph.D. Thesis, McMaster University, Hamilton (1977).
17. D. J. GREEN and P. S. NICHOLSON, "An International Symposium on Fracture Mechanics of Ceramics", edited by R. C. Bradt, D. P. H. Hasseman and F. F. Lange, (Plenum, 1978).
18. E. E. UNDERWOOD, "Quantitative Microscopy", edited by DeHoff and Rhines (McGraw-Hill (1966), 1968) pp. 149.
19. U. F. KOCKS, *Acta Met.* **14** (1966) 1629.
20. Z. HASIN and S. SHTRIKMAN, *J. Mech. Phys. Solids* **11** (1963) 127.
21. V. SATO and J. FURAKAWA, *Rubber Chem. Tech.* **36** (1963) 1081.
22. D. P. H. HASSELMAN and R. M. FULRATH, *J. Amer. Ceram. Soc.* **47** (1964) 52.
23. S. M. WIEDERHORN, A. M. SHORB and R. L. MOSES, *J. Appl. Phys.* **39** (1968) 1572.

Received 22 August and accepted 9 October 1978.